

Unveiling sulfur vacancy pairs as bright and stable color centers in monolayer WS₂

Received: 18 March 2024

Accepted: 25 October 2024

Published online: 02 November 2024

Check for updates

Huacong Sun^{1,2,8}, Qing Yang^{1,8}, Jianlin Wang^{1,2,8}, Mingchao Ding^{1,2,3,8}, Mouyang Cheng^{3,8}, Lei Liao^{1,2}, Chen Cai^{1,2}, Zitao Chen^{1,2}, Xudan Huang^{1,2}, Zibing Wang^{1,2}, Zhi Xu⁴, Wenlong Wang^{1,2,4}, Kaihui Liu^{3,4,5}, Lei Liu^{5,6}, Xuedong Bai^{1,2,4}✉, Ji Chen^{3,5,7}✉, Sheng Meng^{1,2,4}✉ & Lifan Wang^{1,2,4}✉

Color centers, arising from zero-dimensional defects, exploit quantum confinement to access internal electron quantum degrees of freedom, holding potential for quantum technologies. Despite intensive research, the structural origin of many color centers remains elusive. In this study, we employ in-situ cathodoluminescence scanning transmission electron microscopy combined with integrated differential phase contrast imaging to examine how defect configuration in tungsten sulfide determines color-center emission. Using an 80-kV accelerated electron beam, defects were deliberately produced, visualized, excited in situ and characterized in real time in monolayer WS₂ within hBN|WS₂|hBN heterostructures at 100 K. These color centers were simultaneously measured by cathodoluminescence microscopy and differentiated by machine learning. Supported by DFT calculations, our results identified a crucial sulfur vacancy configuration organized into featured vacancy pairs, generating stable and bright luminescence at 660 nm. These findings elucidate the atomic-level structure-exciton relationship of color centers, advancing our understanding and quantum applications of defects in 2D materials.

Color centers, which are defects in crystals, enable single-photon emission, holding significant potential for quantum information technology¹. Among these, color centers in transition metal dichalcogenides (TMDCs) garner intense interest due to their tunable emission properties, high photon extraction efficiency, and seamless integrability^{2,3}. Extensive research has focused on enhancing color centers in WS₂, WSe₂, and MoS₂ through methods like strain engineering and helium ion irradiation^{4–8}. Two types of quantum emitters in TMDCs have been proven: strain-induced localized excitons and transitions involving localized defect states (donor or acceptor levels induced by chalcogen or transition metal vacancies) within the

bandgap⁹. However, the utility of these defect emitters is hindered by spectral instability, including spectral diffusion, blinking, and bleaching^{10–12}. Establishing the correlation between the atomic structure origin of color centers and stable defect emission in TMDCs is demanded for their effective use in quantum technologies.

Identifying color-center origins and optimizing their optical performance is challenging. Photoluminescence (PL) spectroscopy offers high-energy resolution but limited spatial resolution due to diffraction limit^{13–16}. Super-resolution optical techniques like scanning near-field optical microscopy (SNOM) and photoactivated localization microscopy (PALM) localize radiative emission but lack direct correlations

¹Beijing National Laboratory for Condensed Matter Physics, Institute of Physics, Chinese Academy of Sciences, Beijing, China. ²School of Physical Sciences, University of Chinese Academy of Sciences, Chinese Academy of Sciences, Beijing, China. ³School of Physics, Peking University, Beijing, China. ⁴Songshan Lake Materials Laboratory, Dongguan, China. ⁵Interdisciplinary Institute of Light-Element Quantum Materials and Research Center for Light-Element Advanced Materials, Peking University, Beijing, China. ⁶School of Materials Science and Engineering, Peking University, Beijing, China. ⁷Frontiers Science Center for Nano-Optoelectronics, Peking University, Beijing, China. ⁸These authors contributed equally: Huacong Sun, Qing Yang, Jianlin Wang, Mingchao Ding, Mouyang Cheng. ✉e-mail: xdbai@iphy.ac.cn; ji.chen@pku.edu.cn; smeng@iphy.ac.cn; wanglf@iphy.ac.cn

with structural characteristics like strain or defect configuration^{17,18}. High-angle annular dark-field (HAADF) and integrated differential phase contrast (iDPC) imaging in a scanning transmission electron microscope (STEM) has advanced defect structure characterization in MoS₂ and WS₂^{19–22}. These atomic-resolution images distinguish individual defect structures in low-dimensional materials. However, many transmission electron microscopes (TEMs) lack optical detection capabilities, limiting the correlation of optical signatures with structural properties.

Cathodoluminescence (CL), a technique for mapping luminescence in spatial dimensions, has recently been integrated into electron microscopy. Most CL is performed in scanning electron microscopy (SEM), but it faces spatial limitations due to beam broadening and probe size^{23–25}. STEM-CL significantly improves spatial resolution, enabling nanoscale imaging²⁶. The use of a cryogenic stage in this system further minimizes thermal quenching effects, enhancing the CL signal yield and achieving an energy resolution of 0.5 meV. In two-dimensional materials, STEM-CL has been reported to examine the effects of interfaces such as wrinkles and bubbles on optical properties^{27,28}. It has also facilitated the establishment of correlations between quantum emission and strain in hBN²⁹, providing valuable nanoscale insights into microstructure-property relationships.

In this study, STEM-CL and machine learning were employed to further investigate the atomic structural origins of color centers. Monolayer WS₂, recognized for its potential as a single-photon emitter^{30–32}, was chosen and sandwiched between two 20-nanometer thick hexagonal boron nitride (hBN) sheets. This setup enhanced the CL yield by leveraging the quantum well structure (Methods)^{27,33}. The resulting heterostructure was placed on a cryogenic STEM-CL sample stage. The STEM electron beam was utilized simultaneously for three purposes: producing color centers, achieving atomic-level resolution imaging of color centers, and exciting color centers. Concurrently, exciton spectra were collected through CL spectroscopy for in-depth in situ analysis (Methods). During these experiments, hundreds of defect emission spectra, along with their corresponding atomic structures, were collected. This data was subsequently fed into a machine learning algorithm, facilitating a nuanced distinction between color-center configurations that are beneficial or detrimental to the luminescent properties of defects.

Results

Defect emitters in monolayer WS₂

The experimental setup is illustrated in Fig. 1a (Methods). STEM images were captured using a high-angle annular dark-field (HAADF) detector. Depth-sectioning HAADF imaging was employed to locate the position and capture the atomic structure of monolayer WS₂ encapsulated in hBN sheets (Supplementary Fig. 1). The thus focused incident 80 kV accelerated electron beam excites the monolayer WS₂, resulting in the emission of CL spectra. The initial monolayer WS₂ sample exhibits a flawless crystalline lattice and an intrinsic edge-band exciton (A^0) peak at 620 nm without notable defects (Supplementary Fig. 2). By intentionally positioning the focused electron beam on different regions of the WS₂ and varying the dwell time, defects were deliberately introduced due to radiolysis effect (Methods).

Subsequent CL spectral mapping of these defects, after filtering out the intrinsic band-edge luminescence, clearly illustrates the location of the in situ-generated color centers, as depicted in Fig. 1b. Figure 1c shows the emission spectra corresponding to different regions in Fig. 1b. Clearly, the unirradiated region I exhibits a neutral exciton (A^0) peak at 620 nm, which is consistent with the reported bandgap of monolayer WS₂ (2.0 eV), as shown in region I in Fig. 1c. In contrast, regions II and III, which were irradiated, exhibit new peaks labeled as X_L at 668 nm and 663 nm, respectively, each with a full width at half maximum (FWHM) of approximately 35 meV. Notably, region III, which

received the mostly radiation, shows significantly enhanced CL emission with a much larger intensity ratio of X_L/A^0 .

It is worth noting that defect emissions within the visible frequency range, spanning from 540 to 735 nm, have been reported active in hBN at room temperature due to deep defect states^{29,34,35}. In contrast, defect-induced emissions in WS₂ have only been observed at cryogenic temperatures⁹. To affirm the source of the observed exciton emission, temperature-dependence CL measurements were conducted. The appearance of the X_L emission peak at 660 nm, observed with decreasing temperature in the hBN|WS₂|hBN heterostructure, in contrast to the persistently dark hBN area, conclusively confirms that the defect emission here does not originate from hBN (Supplementary Fig. 3). Furthermore, the current electron beam irradiation does not induce carbon doping as reported in previous studies, and the observed peak positions differ from those in carbon-doped hBN³⁶, consistently corroborating that the experimentally observed spectra originate from WS₂. The effect of dielectric screening due to hBN encapsulation should also be considered, as it shifts emission energy³⁷, causing a redshift in TMDC defect emission peaks and affecting neutral exciton and trion peaks¹⁵. We extracted the difference between the defect and neutral exciton peaks to decouple from the peak shifts induced by hBN encapsulation.

The in situ HAADF images further show the structural origin details of the color centers (Fig. 1d). In the Z-contrast HAADF micrographs, the bright spots correspond to the position of the W atom ($Z=74$), while the S columns remain invisible due to their lower atomic number ($Z=16$) and thus lower scattering power. Intriguingly, distinct lattice distortions were observed at the color centers, as evidenced by a reduction in the spacing between W atoms to 3.03 Å, in contrast to the unaltered pristine lattice, which aligns with the single-crystalline value of 3.18 Å. For added clarity, the W atomic distance mapping was measured and superimposed onto the HAADF image (Supplementary Fig. 4). As shown in Fig. 1d, several instances of lattice shrinkage, approximately 4.7% in magnitude (highlighted by blue triangles), are discernible at the color centers. Through the quantitative analysis of W atom distortions in the subsequent sequential HAADF images, seven types of arising defects induced by electron-beam irradiation were classified, as shown in Fig. 1e. Data comprising defect types and quantities, extracted from the HAADF images along with the corresponding defect emission spectra, were then integrated into the machine learning framework. This integration was employed to elucidate the atomic structural origins of distinct color centers, as documented in Fig. 1f, g.

Fabrication and identification of defects

To verify the repeatability of the atomic defect configuration caused by electron beam irradiation, we used in situ iDPC imaging with full-element atomic resolution to record the defect generation process in a free-standing monolayer WS₂ for comparison, as shown in Fig. 2.

Figure 2a presents an atomic-resolution iDPC image of a pristine monolayer WS₂, showcasing well-connected W-S hexagonal rings devoid of any defects. As the cumulative electron beam dose increases during continuous iDPC imaging, radiolysis-induced sulfur vacancies become apparent. This is attributed to the energy transferred to sulfur atoms by high-energy electrons, surpassing the 2.1 eV knock-on displacement threshold¹⁹. Consequently, Fig. 2b reveals four distinct defect configurations, delineated by white dashed lines, including single sulfur vacancies (V_{1S} , Type I), disulfide vacancies (V_{2S} , Type II), sulfur vacancy pairs in immediate proximity (Type III), and three linear adjacent V_{1S} configurations (Type IV).

The accumulation of electron radiolysis during in situ imaging led to the increased aggregation of sulfur vacancies in WS₂, as illustrated in Fig. 2c. This aggregation resulted in the formation of inverted triangles (Type V), right triangles (Type VI), and chains (Type VII), each composed of sulfur vacancies in adjacent rings. Utilizing the atomic

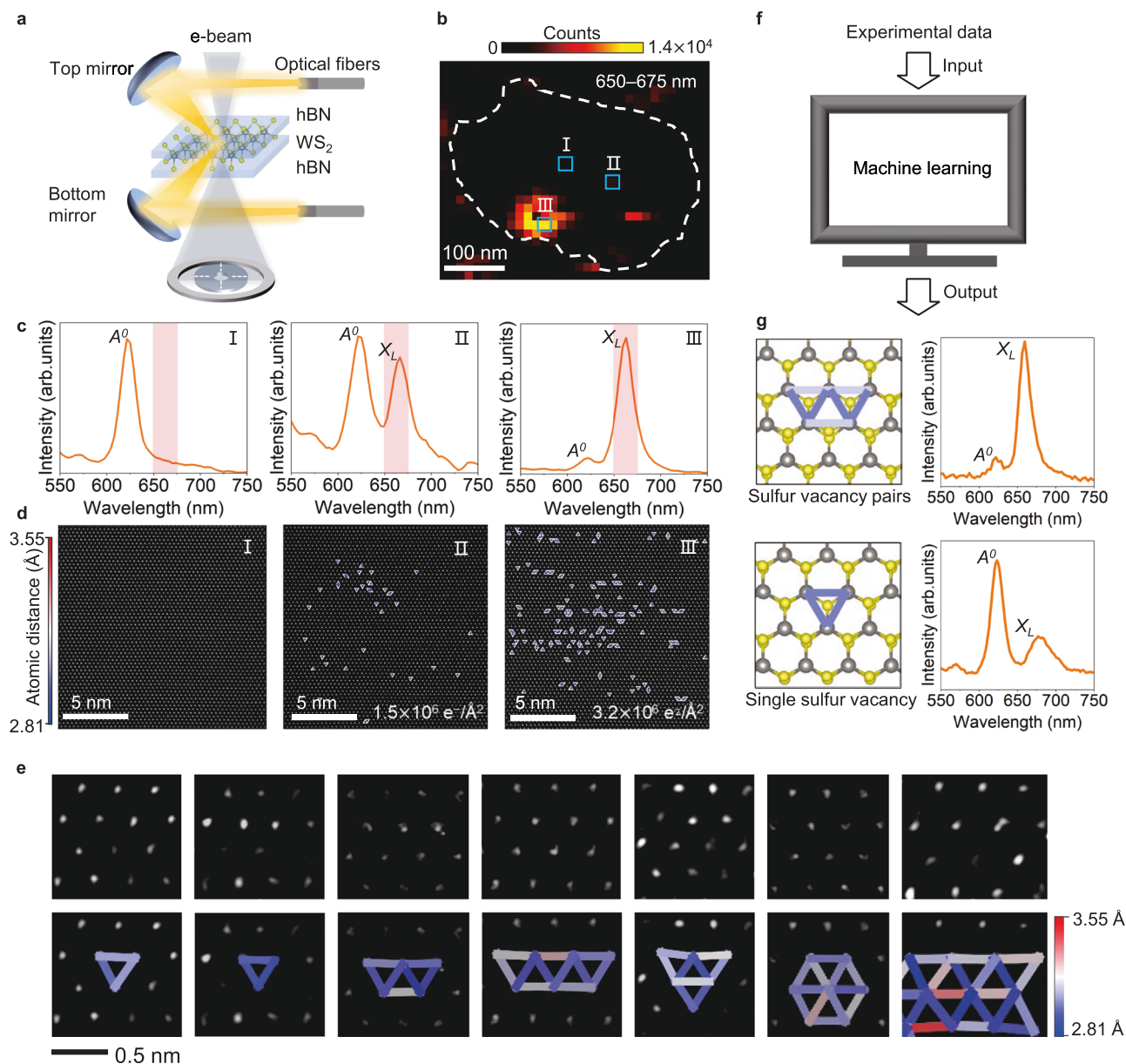


Fig. 1 | Correlated optical and structural characterizations of defect emitters in hBN|WS₂|hBN heterostructures. **a** Schematics of the scanning transmission electron microscopy cathodoluminescence (STEM-CL) experiment setup. Electron beam excites the heterostructure to emit CL which is reflected by two parabolic mirrors to optical fibers. The transmitted electron beam is collected by the segmented detector (inner) or high-angle annular dark-field (HAADF) detector (outer). **b** CL spectrum mapping of an electron-beam radiated hBN|WS₂|hBN heterostructure with a wavelength window of 650–675 nm, showing the position of color centers formed with varying electron-beam radiation durations. The white dotted line circles the suspended area of a hBN|WS₂|hBN heterostructure on a TEM grid. **c** CL spectrum of region I, II, III in **b**. The red boxes in **c** indicate the wavelength window of 650–675 nm. A^0 denotes the peak position of intrinsic edge-band

exciton, while X_L signifies the peak position of the localized defect exciton. **d** High-magnification STEM-HAADF image of monolayer WS₂ in region I, II, III in **c** overlapped with tungsten atom distance mapping, showing atomic-resolution structural origins of the defect emission. Only distorted areas are marked in the mapping. **e** High-magnification STEM-HAADF images of the emerging defects and corresponding tungsten atomic distance mappings of monolayer WS₂ in **b**, showing seven types of defects arising due to long-time continuous electron beam radiolysis. **f** Schematic diagram of data analysis using machine learning, where the input consists of 101 sets of defect emission spectra and corresponding atomic structures. **g** Machine learning output results, indicating that the impact of sulfur-vacancy pairs on the optical properties of defect emissions differs from other color centers. Defects are overlaid with tungsten atom distance mapping.

configurations of defects obtained during in situ fabrication, we conducted a quantification analysis of the corresponding lattice distortions, specifically focusing on the tungsten atomic spacing. The in situ STEM-IDPC images of the monolayer WS₂ in Fig. 2d show the emergence of seven defect species due to electron beam radiolysis, consistent with in situ STEM-HAADF imaging of encapsulated WS₂. The corresponding lattice distortions were established, as depicted Fig. 2e. Both the distortion magnitude and shape of the defect species are identical to those observed in encapsulated monolayer WS₂ and in

free-standing monolayer WS₂ observed by HAADF imaging (Fig. 2f–h and Supplementary Fig. 5), elucidating a similar defect formation scenario for both encapsulated and free-standing monolayer WS₂ under electron beam radiolysis.

Theoretical calculations were conducted to further investigate the influence of hBN encapsulation on defect formation and evolution in monolayer WS₂ under electron beam radiolysis (Methods, Supplementary Table 1, Supplementary Fig. 6). Our findings indicate that the formation energy of sulfur vacancies in free-standing monolayer WS₂ is

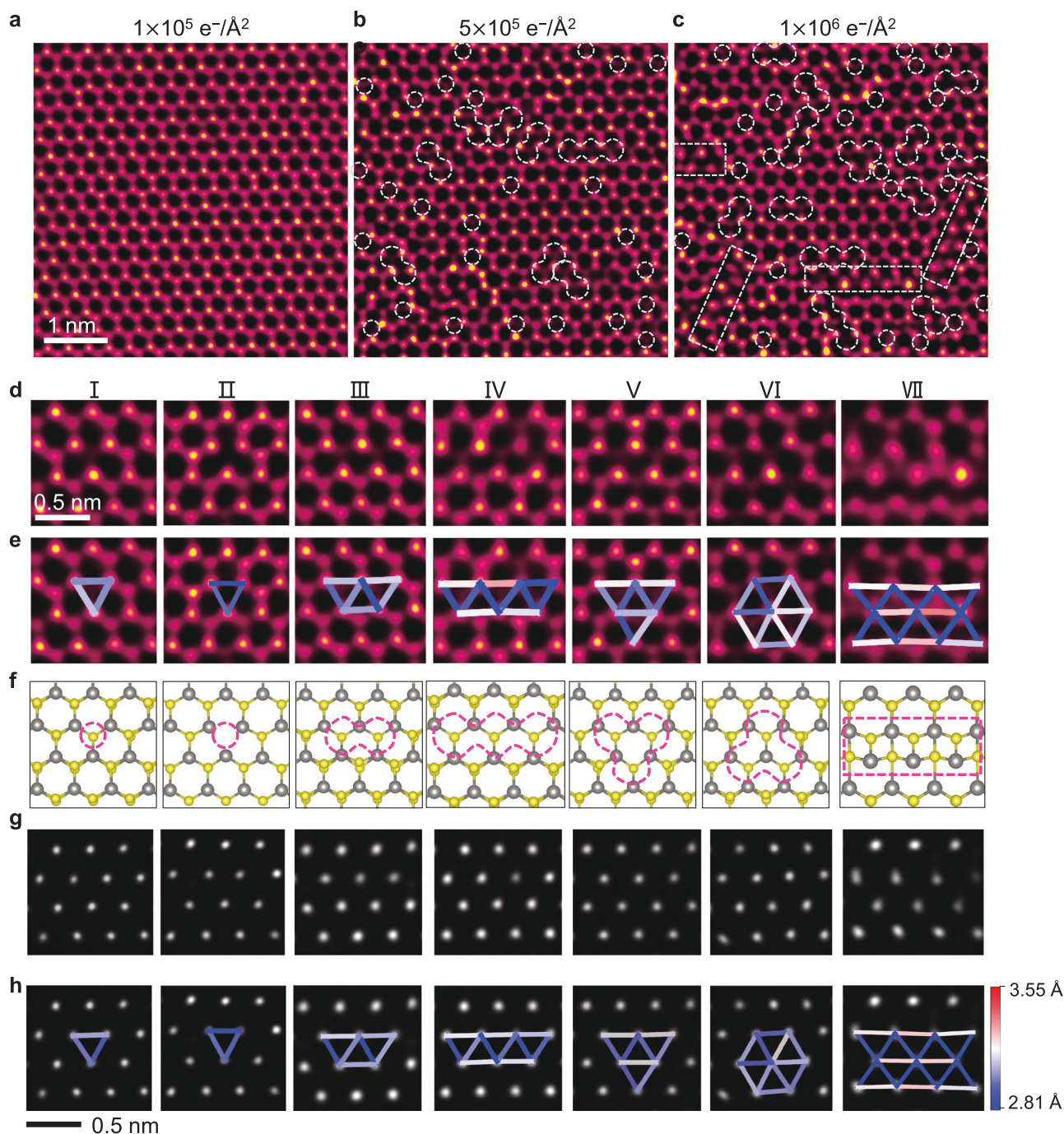


Fig. 2 | Fabrication and scanning transmission electron microscopy integrated differential phase contrast (STEM-iDPC) imaging of atomic defect configurations in free-standing monolayer WS₂. **a–c** Sequential STEM-iDPC image of a free-standing monolayer WS₂. Defects introduced due to beam radiolysis are marked by white dashed lines. **d** High-magnification STEM-iDPC images of all defect species arising due to electron beam probing. In a left-to-right sequence, I: single sulfur vacancy (V_{1S}); II: disulfide vacancy (V_{2S}); III: paired-sulfur vacancy; IV: triplet sulfur

vacancy; V, VI: two types of sulfur vacancy cluster; VII: sulfur vacancy chain. **e** Lattice measurements of **d**. **f** Corresponding atomic structure model of defect configurations in **e**. Sulfur vacancies are marked by dashed circles. **g, h** Simultaneous STEM-HAADF images of all defect configurations in free-standing WS₂, along with corresponding lattice distortion measurements, showing agreement with iDPC images and experimental results for encapsulated monolayer WS₂.

3.34 eV. In hBN-encapsulated WS₂, this energy converges to 3.43 eV when the encapsulation thickness exceeds two layers, resulting in a difference of 0.09 eV. Additionally, Monte Carlo (MC) simulations indicate that at a temperature of $T = 102$ K and an energy difference of 0.09 eV, defects are generated 10,000 times more slowly in the hBN-encapsulated WS₂ compared to free-standing WS₂ under the same electron beam irradiation conditions (Supplementary Fig. 7). This

finding qualitatively aligns with our experimental observations. Given the exponential dependence of the formation rate ratio on energy and temperature, fluctuations in the electron beam dose and temperature during different experiments may cause variations in the reaction rate ratio for the same defect formation.

The variations in defect distortions within the surrounding lattice ranged from 4.7% (Type I) to 16.3% (Type VII) for different defect

species. Thus, a straightforward and unequivocal atomic-resolution correlation emerged between the defect configuration and lattice distortion across different scales. This, in turn, provides compelling and distinctive evidence for distinguishing between different defect configurations in our experiments. Accordingly, we delved into exploring the relationship between the defect structure and the optical properties of radiolysis-fabricated color centers in monolayer WS₂.

Correlated optical properties and atomic configurations

The in situ, real-time generation of defects, along with the concurrent collection of CL spectra and HAADF images, is detailed in Fig. 3. As depicted in Fig. 3a, four distinct optical signatures emerged sequentially: X_L emission, spectral diffusion, emission with exceptional color purity, and spectral bleaching. The corresponding CL spectral evolution in Fig. 3b further shows the defect emission peak shift with varying intensity and FWHM, implying the influence of defect intensity and species diversity on the emission properties. The time evolution of the central peak positions and the intensities of both the neutral exciton and defect emission peaks are depicted in Fig. 3c. The simultaneously acquired HAADF images in Fig. 3d reveal the respective defect structures, with each type marked with distinct colors, based on atomically measured lattice distortions using tungsten atomic coordinates.

When comparing the spectrum with the real-space defect quantification image, it becomes evident that in the initial stage, with isolated sulfur vacancy defects present, the exciton state exhibits sporadic luminescence accompanied by spectral diffusion, ranging from 642.3 nm to 694.1 nm, and the integral defect emission intensity is lower than the A^0 peak. Previous studies proposed that localized emission in TMDCs results from excitons trapped in anion vacancies^{15,16,30,38,39}. Our findings show that emissions linked to isolated sulfide vacancies display significant emission diffusion and structural instability. Discrete single vacancies have been reported and also observed in our experiments to be mobile under the electron beam illumination, supported by theoretical calculations (Supplementary Figs. 6 and 8)^{19,40}. The hopping behavior of V_{1S} would lead to local fluctuating electromagnetic fields and a variational dielectric environment, which is responsible for spectral diffusion¹¹. This energy instability hinders photon coherence, affecting the quality of two- or multiphoton entanglement and, thus, their utility in quantum information science.

Remarkably, a high concentration of type III defects, specifically paired-sulfur vacancies in WS₂ ($t = 900$ s), yields a stable and brilliantly bright X_L emission at 660 nm with high color purity. This emission exhibits a narrow FWHM of 22 nm and an intensity 2.4 times stronger than the A^0 peak. In contrast, the emergence of disulfide vacancies (V_{2S} , Supplementary Fig. 9), triadic sulfur vacancies, sulfur vacancy chains, and tungsten vacancy defects ($t = 1200$ s) results in blinking and bleaching of the emitted light, commonly observed in previous studies. The defect peak shifts to 666.5 nm with a slightly increased FWHM of 26 nm. Due to the appearance of blinking and bleaching phenomena, the intensity peak ratio $I(X_L)/I(A^0)$ decreases to 1.4. Blinking is reported due to nonradiative recombination, caused by one or both of the excited carriers escaping to the surface¹², while spectral bleaching results from photochemical reactions or material degradation^{41,42}. Given these characteristics, defects belonging to Types II, IV–VI demonstrates their adverse impact on emission properties.

The statistical analysis of the sequential emergence of defects in monolayer WS₂ is presented in Fig. 3e. In the order of their appearance, the quantities of Type I defects, Type III defects, and the cumulative quantity of the remaining six defect types are plotted over time in Fig. 3f. Clearly, in the presence of type III defects, particularly sulfur vacancy pairs in the immediate vicinity, emissions are bright and stable, highlighting their advantageous role as color centers in hBN-encapsulated WS₂. This finding is further supported by the comparison

of STEM-CL results for samples with similar sulfur vacancy densities but varied proportions of Type I and Type III defects. The results show that samples with a higher proportion of Type III defects exhibit better defect luminescence, indicated by a higher X_L/A^0 ratio. (Supplementary Fig. 10).

By means of electron beam irradiation, the modulation of defects in monolayer WS₂ results in the inevitable generation of isolated sulfur vacancies. As the defect density increases, the proportion of sulfur vacancy pairs rises, accompanied by the generation of more types of aggregated sulfur vacancy complexes. (Supplementary Fig. 11). In order to comprehend complex, non-linear relationships and interactions among multiple defect types, which can significantly influence luminescence properties, a machine learning model was trained on direct experimental data. Our dataset comprises over one hundred independent experimental measurements of defect CL emission and corresponding W atomic coordinates. Utilizing the number of distinct defect types extracted from W atomic coordinates in STEM images as input features, we trained an XGBoost model to predict the emission intensity peak ratio $I(X_L)/I(A^0)$ (Methods). The predictions of our trained model are illustrated in Fig. 3g, covering typical defect counts for Types I & III. Given the dominance of Types I & III defects, we omitted the contribution of other defects in this analysis. The results clearly indicate that Type III defects favor a larger intensity ratio, while Type I defects tend to disrupt the defect spectrum peak $I(X_L)$.

It is noteworthy that the increase in defect density in the initial stages of defect formation leads to a decrease in neutral exciton peak intensity while enhancing defect emission in WS₂, consistent with previous studies^{43,44}. Our in situ STEM-CL quantifications indicate a defect density of 8.58×10^{13} cm⁻² in monolayer WS₂ encapsulated by hBN, demonstrating optical defect emission characterized by the maximum proportion of sulfur vacancy pairs.

Additionally, it has been reported that nanoscale strain in 2D materials influences their CL emission²⁹. It is therefore essential to consider the impact of strain as defect density increases. In our study, defects with inherent local atomically distortion, evenly and gradually generated in monolayer WS₂ encapsulated in hBN nanosheets, introduce evenly distributed atomically localized strain. This results in distinct behaviors of strain distribution and defect emission compared to systems with uneven strain distribution and associated emission (Supplementary Fig. 12).

Band structure and transition elements of WS₂ color centers

Based on the identified defect atomic configurations, first-principles calculations of $7 \times 7 \times 1$ supercells were performed to investigate the electronic band structure of different color centers in WS₂. The pristine monolayer WS₂ (Fig. 4a), displays a direct bandgap at the high-symmetry K-point (Fig. 4b, 4c), which corresponds to the experimental neutral exciton emission (A^0) at 2 eV. The introduction of type III defects (Fig. 4d) creates four unoccupied defect states within the gap, referred to as C_{D1} , C_{D2} , C_{D3} , and C_{D4} (Fig. 4e). The shallowest defect state, C_{D4} , located at 0.11 eV below the conduction band minimum (CBM), closely aligns with the experimental 0.13 eV peak separation between the bright X_L emission and the A^0 emission. This suggests that transitions between C_{D4} and the valence band maximum (VBM) of type III defects are responsible for the stable and bright X_L emission at 660 nm, in agreement with experimental results.

Transition matrix element calculations reveal that at the K-point, the VB- C_{D4} transition probability is significantly higher than the transition probability to the other three defect states (C_{D1} , C_{D2} , C_{D3}), as depicted in Fig. 4f. The combined linear contribution of the squares of transition matrix elements and electronic density to luminescence intensity provides additional confirmation that sulfur-vacancy pairs are the structural origin of stable and bright defect luminescence in monolayer WS₂ (Methods, Supplementary Fig. 13, Supplementary Table 2).

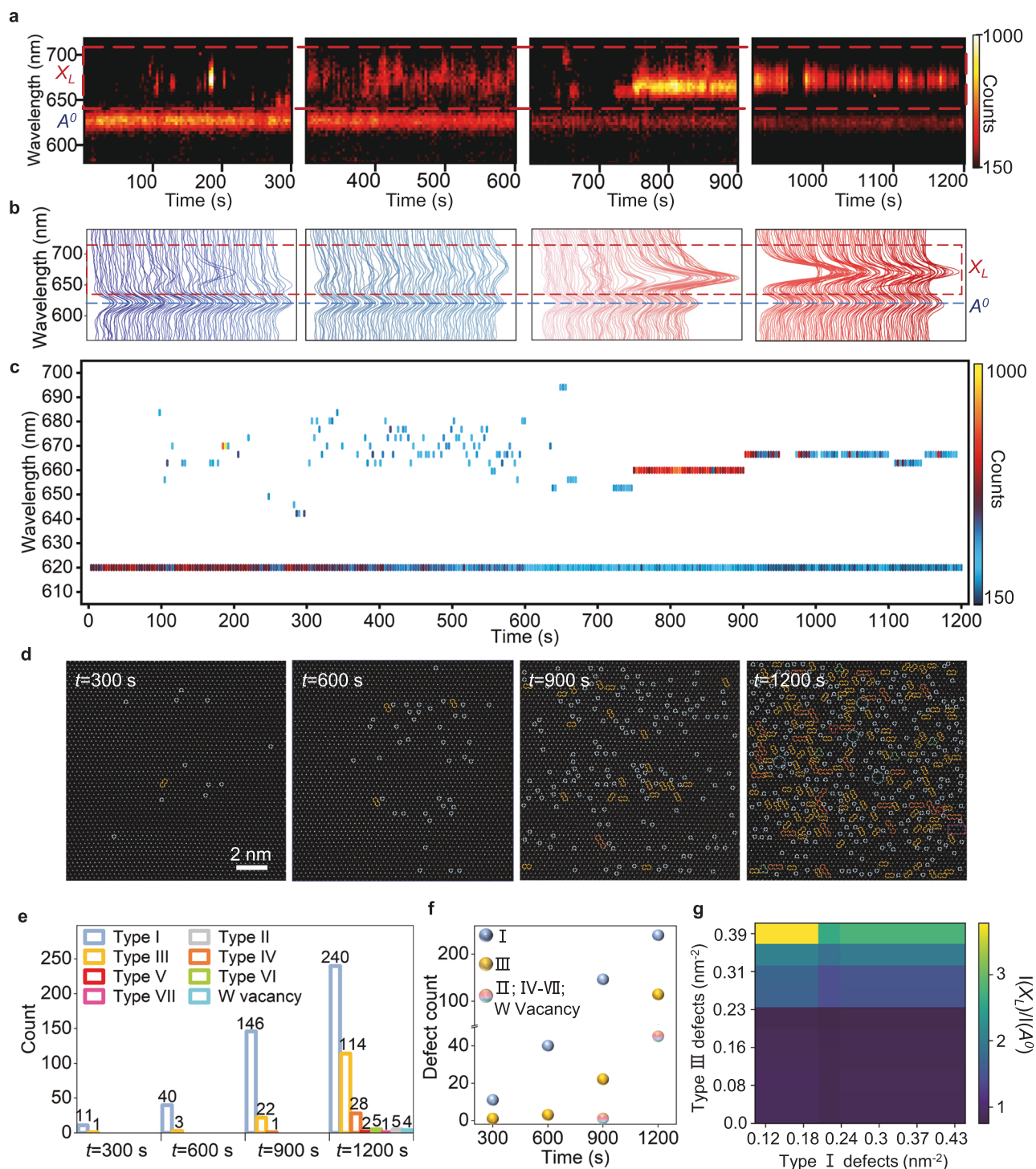


Fig. 3 | Evolution of optical properties and the corresponding color-center configurations in hBN | WS₂ | hBN heterostructures. **a** Real-time in situ tracking of defect luminescence in a hBN|WS₂|hBN heterostructure with a 3-second interval over four 300-second periods. Evolution of defect emission in optical properties: emergence, spectral diffusion, stable and bright emission, and blinking and bleaching. **b** Corresponding CL spectra in **a**. The red dashed box indicates the peak position range of defect exciton (X_L) emissions, while the blue dashed line represents the peak position of neutral exciton (A^0) emissions. **c** The plot of peak position

and peak intensity of A^0 emission and X_L emission as a function of irradiation time in **a**. **d** Simultaneous in situ sequential atomic-scale STEM-HAADF images of the WS₂ sample with the measurement timing noted as in **a** and **b**. Different defect types are marked with distinct colors. **e** Defect types and quantity statistics in **c** at four different time points: $t = 300$ s; 600 s; 900 s; and 1200 s. **f** Evolving defect concentrations statistics in **d**. **g** Machine learning generated heatmap illustrating the joint effects of Type I & III defect counts on the relative emission intensity $I(X_L)/I(A^0)$.

It is noted that, for single sulfur vacancy configuration (Type I), primary transitions occur from the VB to the CB, not the defect states. Similarly, two discrete sulfur vacancies lead to four nearly degenerate unoccupied defect states within the bandgap, located at 0.43–0.48 eV

below the conduction band. This illustrates that the hybridized states depend on the defect-defect interaction, introducing additional trap states via the hybridization of individual vacancy levels⁴⁵. Transition matrix element calculations further show the primary transitions for

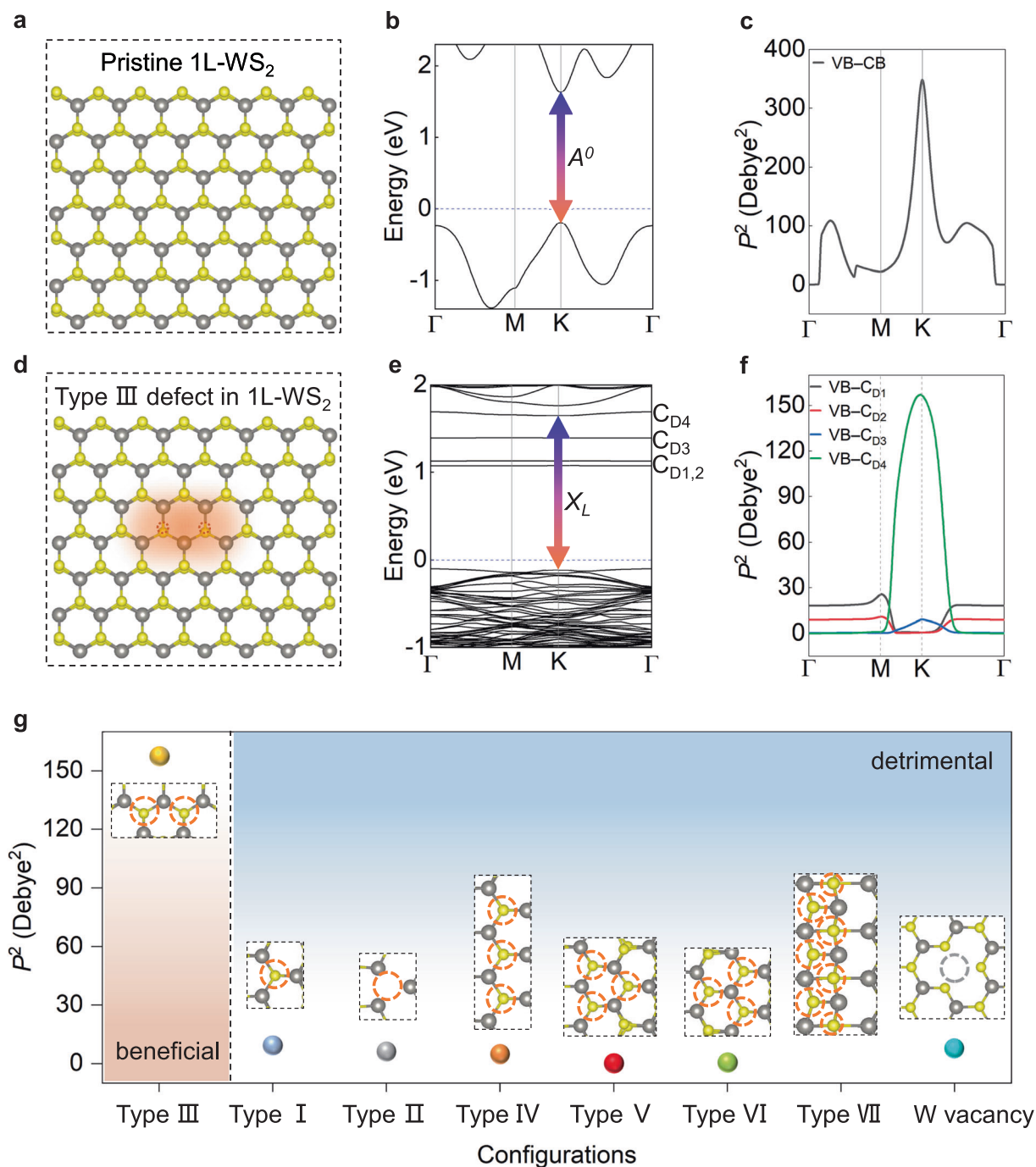


Fig. 4 | Calculated electronic band structure and corresponding transition matrix elements (P^2) of different color-center configurations in monolayer WS_2 . **a** Top view of a 7×7 supercell of pristine monolayer WS_2 . **b, c** Computed electronic band structures of pristine WS_2 (**b**) and corresponding transition matrix elements from the valence band (VB) to the conduction band (CB) across the Brillouin zone (**c**). **d** Top view of a 7×7 supercell with one sulfur vacancy pair. Sulfur vacancies are marked by orange dashed circles. **e** Calculated electronic band structures of **d**. Defect states are labeled as C_D for unoccupied states. **f** Transition matrix elements from the valence band to C_D . The inset arrows in **b** and **e** represent

the transition with the highest probability, as determined through the analysis of the transition matrix element. **g** Dependence of P^2 value on color-center configurations for the transition between the localized defect state (nearest to the conduction band) and the valence band maximum at the K point. The inset shows corresponding defect configurations. Sulfur vacancies are marked by orange dashed circles, and W vacancies are marked by gray dashed circles. The orange-shaded areas highlight defect configurations that are favorable for stable and bright luminescence, whereas the blue-shaded areas represent detrimental color centers.

discrete sulfur vacancies continue to be dominated by VB–CB transitions, demonstrating weak defect emission (Supplementary Fig. 14).

The band structure and transition matrix elements for other experimentally observed defect configurations are detailed in Supplementary Fig. 15. In particular, transition matrix elements between the localized defect state (closest to the conduction band) and the

valence band maximum at the high-symmetry K-point, for all configurations, except type III, consistently remain below 10, indicating the dominance of band-edge transition, as illustrated in Fig. 4g. Configurations involving three or more clustered sulfur vacancies result in the splitting of defect impurity levels, creating multiple deep unoccupied defect states that trap carriers⁴⁶, negatively impacting radiative

recombination. In contrast to sulfur vacancies, tungsten vacancies introduce acceptor energy levels. However, transitions involving defect states are still limited, with a predominance of transitions between the VB and CB. Sulfur-vacancy chains (Type VII), which possibly cause WS₂ degradation, narrow the bandgap to 0.2 eV, adversely affecting emission properties. These findings align with experimental observations of bleaching.

Optical characterization of defects luminescence

PL results indicate that the color centers fabricated in WS₂ exhibit both brightness and stability. However, under electron radiation, the formation of sulfur-vacancy pairs consistently occurs in conjunction with the presence of sulfur vacancies. Consequently, the attainment of a pure and isolated paired-sulfur vacancy defect has proven to be unattainable. This limitation is evident in photon measurements, where $g^2(0) = 1$ shows the random characteristics of the emitted photons (Supplementary Fig. 16). Further investigation into refined preparation methods holds the potential to facilitate controlled single-photon emission in the future.

The engineering of color centers inevitably gives rise to a diverse array of defect species, with some exhibiting optical activity, while others do not luminesce but rather alter the local dielectric environment, thereby influencing emissions. In this study, we harnessed in situ STEM-CL, machine learning, and DFT calculations to unequivocally unveil, at the atomic scale, the distinct spectral origins and roles of defect species in monolayer WS₂. Our research unambiguously demonstrates the pivotal role of sulfur-vacancy pairs in WS₂ as the stable color centers. Conversely, various other defect types, such as single sulfur vacancies, triadic sulfur vacancies, sulfur vacancy chains, and tungsten vacancies, have been identified as detrimental sources of spectral instability. Our work provides atomic-scale insights into the structural origins of defect excitons, offering a pathway for the identification of defect emitters and enabling their application in single-photon sources for quantum technologies through the intentional design and precise atomic-scale engineering of defects.

Methods

Sample preparation

A modified dry transfer technique using polypropylene carbonate (PPC) is carried out to fabricate the hBN|WS₂|hBN heterostructure⁴⁷. The PPC film was used to first pick up the 20nm-thick hBN flake that exfoliated from hBN bulk crystals (Shanghai Onway Technology), then the monolayer WS₂ exfoliated from WS₂ bulk crystals (HQ graphene), and subsequently the 20 nm-hBN flake under 40 °C in sequence. After annealing at 200 °C on silicon substrate for 8 h, the heterostructure sample was released on a TEM copper grid at 130 °C. The sample was further sequentially cleaned by acetone, isopropanol, and nitrogen gas annealing to remove the residues and increase the adhesion between the sample and the TEM grid.

STEM-CL characterization

The JEOL JEM-ARM300F transmission electron microscope (TEM) was operated at an electron-accelerating voltage of 80 kV. The microscope is equipped with a Gatan Vulcan cathodoluminescence (CL) system for simultaneous STEM and CL measurements. The Gatan Vulcan CL holder featured two miniature elliptical aluminum mirrors positioned both above and below the sample, allowing for light collection at an angle of up to 7.2 steradians. These elliptical mirrors couple the light to two optical fibers directed toward a photomultiplier tube (PMT) or charge-coupled device (CCD) for detection. Simultaneously, scattered electrons from incoherent interactions with the materials are collected by the HAADF detector for real-space imaging. Software drift correction (after every 20 pixels) was on during the collection to address potential drift issues. All STEM-CL characterization experiments were conducted at 102 K, except for the temperature-dependent

experiments shown in Supplementary Fig. 3. Data collection and analysis were performed using a Digital Micrograph.

Extrinsic defect fabrication

Color centers were fabricated by parking transmitted STEM electron beam spot on different regions of WS₂ in the prepared hBN|WS₂|hBN heterostructures with different dwell times in few seconds' range. The incident electron beam current was used at 0.73 nA (1c).

Subsequently, the incident electron beam of the microscope was then converged to 0.14 nm with a convergence angle -18 mrad with 30 μm condenser lens aperture to scan the sample and stimulate the CL signal. The incident electron beam current is 0.285 nA (4c), corresponding to the electron beam dose of $2.73 \times 10^5 e/\text{Å}^2$.

Radiolysis effect

The maximum transferred energy E_{max} from 80 kV incident electrons to the sulfur atom is calculated to be 6 eV. This calculation utilizes the following formula^{48–50}:

$$E = E_{\text{max}} \sin^2 \left(\frac{\theta}{2} \right) \quad (1)$$

$$E_{\text{max}} = E_0 \left(1.02 + \frac{E_0}{10^6} \right) / (465.7A) \quad (2)$$

Where E_0 represents the incident electron energy in electronvolts (eV), A is the atomic mass number, and θ is the electron deflection angle. In the case of collision with the nucleus, $\theta = 180^\circ$ and thus $E = E_{\text{max}}$.

STEM-depth-sectioning imaging

STEM-depth-sectioning technique⁵¹ was utilized to image the monolayer WS₂ encapsulated in hBN nanosheets. The STEM probe, with a depth of field of 8.33 nm, was adjusted for sectional-depth scanning imaging of layers at different depths. Using this depth-sectioning serial imaging, the location of the monolayer WS₂ encapsulated in thick hBN layers was pinpointed for further in situ STEM-CL experiments.

W atom distance mapping

The position of W atoms in HAADF images was determined using a two-dimensional Gaussian peak-fitting method through a custom MATLAB code⁵². Subsequently, the distances between these W atom columns were calculated from their pinpointed positions using a custom Python script⁵². A W-distance mapping was superimposed on the HAADF image, with line colors denoting the distance values between the W atom. To highlight defects, we depicted the W atomic distance mapping with triangles where the mean length of the three sides was less than 3.03 Å (W atom distance of a single sulfur vacancy).

STEM-iDPC experiments

The sample for DPC characterizations was prepared by transferring monolayer WS₂ onto the TEM grid (Quantifoil) using the polymethyl-methacrylate-based transfer method. The DPC images were acquired using an eight-segment annular detector, coupled to JEOL ARM300F TEM operated at 80 kV, using a STEM probe current below 23 pA. Images were acquired with a camera length of 20 cm, convergence semi-angle of 22.4 mrad, and collection semi-angle ranging from 0 to 27 mrad. The DPC-STEM techniques were used to image the in-plane displacement of the transmitted electrons, while the images were approximately proportional to the projected potential STEM-iDPC. iDPC images were calculated using a custom MATLAB program. Poisson noise was removed using the Bandpass filter.

Image simulations

We utilized xHRTEM™ ver. 4.4, a commercial software, to simulate high-angle annular dark-field (HAADF) images using the multi-slice

method. For the simulation of integrated differential phase contrast (iDPC) images, the QSTEM software was employed⁵³. The simulated images were convolved with a Gaussian function having a full width at half maximum of 0.8 Å to account for the probe size. Relaxed structures of monolayer WS₂ with seven distinct defect configurations were considered. The simulations were conducted under experimental conditions at 80 kV, with a set convergence angle of 22 mrad and a collection angle ranging from 54 to 220 mrad.

Machine learning regression of emission intensity ratio

To generate the training data, we carried out graph clustering analysis on the W sites with defect (extent of lattice distortion greater than 4.7%), and counted the size of each separate cluster. This allows us to generate an input vector for each structure with 3 features: (type I counts, type III counts, and counts for other type defects). The output data for each structure is the ratio of two CL intensity peaks $I(X_i)/I(A^0)$.

For the training process, we implemented the XGBoost model with scikit-learn package^{54,55}. We built a model with 100 estimators along with L1 regularization $\alpha = 0.5$ to ease over-fitting, and we used 85% of the data for training and 15% for testing. The mean squared error loss is optimized on $\log I(X_i)/I(A^0)$ for better performance.

Computational methods

Our density function theory (DFT) calculations were performed based on the Vienna ab initio simulation package (VASP). The exchange-correlation effect was described within the generalized gradient approximation (GGA) in the Perdew–Burke–Ernzerhof (PBE) functional, together with the projector augmented wave (PAW) potentials. The kinetic energy cutoff was set to 500 eV, and the total energy convergence criterion 10^{-6} eV was used. A vacuum space along the *c* direction is larger than 15 Å to avoid spurious interactions. In our simulation, to determine the influence of the vacancy intensity, we used a $7 \times 7 \times 1$ supercell with $W_{49}S_{98}$ to calculate the electronic and optical properties. The optimized convergence criterion for atomic coordinates was less than 0.01 eV/Å for forces on each atom, and the output structure is visualized using VESTA⁵⁶. The dielectric function is defined as $\epsilon(\omega) = \epsilon_1(\omega) + i\epsilon_2(\omega)$, where $\epsilon_2(\omega)$ is the image part, and $\epsilon_1(\omega)$ is the real part of the dielectric function, respectively. We calculated the transition dipole moment (TDM) to analyze the electron excited ratio from the Valence bands (VBs) to the Conduction bands (CBs), which is defined:

$$d_{nm} = \int \psi_n^* \hat{d} \psi_m d^3r = \langle \psi_n | \hat{d} | \psi_m \rangle \quad (3)$$

Linear correlation between the squares of transition matrix elements and luminescence intensity is given by the equation⁵⁷:

$$I(\hbar\omega) = \frac{n_D \omega^3}{3\epsilon_0 \pi c^3 \hbar} |\vec{\mu}_{eg}|^2 \sum_m |\chi_{gm} \chi_{e0}|^2 \delta(E_{ZPL} - E_{gm} - \hbar\omega) \quad (4)$$

$I(\hbar\omega)$ represents luminescence intensity, and $\vec{\mu}_{eg}$ represents transition dipole moment between the excited and the ground state. n_D is the refractive index; χ_{gm} and χ_{e0} are vibrational levels of the excited and the ground state.

The minimum energy path and the migration energy barrier are calculated using the climbing image nudge elastic band (CI-NEB) method^{58,59}. 5 intermediate images are inserted on the transition path of defect migration, and relaxed convergence criterion is less than 0.03 eV/Å for forces on each atom.

For the analysis of the effects of hBN encapsulating layers on the WS₂ monolayer, we stacked an ideal 5×5 WS₂ supercell layer between two 6×6 hBN supercells. The distance between the WS₂ and hBN layers is set to 3.3 Å, and the hBN supercell is strained by less than 10% to match the supercell size of WS₂. Both hBN layers are fixed during

structural relaxation, and we implemented the DFT-D3 van der Waals correction to describe the interlayer interactions⁶⁰. The structure was visualized using VESTA. All DFT calculations were performed using the VASP package. Within this established model, a sulfur atom is removed, and the structure is relaxed to obtain a model with a vacancy. From this model, the total energy of the system with sulfur vacancy was calculated. We took molecular eight-membered alpha-sulfur (S₈) as the sulfur reservoir to determine the chemical potential of the ejected S atom⁶¹. The alpha-sulfur structure was optimized using DFT based on data from the Materials Project⁶², yielding the total energy of the α -sulfur ring.

Thus, the formation energy of a single sulfur vacancy E_f is obtained as

$$E_f = E(\text{vac}) + 1/8E(S_8) - E(\text{ini}) \quad (5)$$

where $E(\text{vac})$ is the total energy of the system with sulfur vacancy, $E(S_8)$ is the total energy of the α -sulfur ring, and $E(\text{ini})$ is the total energy of the pristine system without defects⁶³.

Monte Carlo simulations

A Monte Carlo (MC) simulation was conducted to investigate the time evolution of defect density subjected to an external electron-beam energy source. This simulation takes into account both the defect formation energy (E_f) and the input energy (E_{in}) delivered by an external electron beam, which affects the dynamics of defect formation. The system is modeled as a lattice comprising 2,500 sites where defects can occur.

The transition rates for defect formation are determined using an Arrhenius-type expression, which accounts for the temperature dependence of the reaction rates:

$$\Gamma = \nu(E_{in}) \exp\left(-\frac{E_f}{k_B T}\right) \quad (6)$$

Specifically, the attempt frequency $\nu(E_{in})$ is enhanced in accordance with

$$\nu(E_{in}) = \nu_0 \exp(E_{in}/k_B T) \quad (7)$$

where ν_0 is the intrinsic attempt frequency constant, k_B is the Boltzmann constant, and T is the temperature. The simulation progresses through a series of Monte Carlo steps, during which the probability of defect formation at each site is determined, and the lattice is updated accordingly.

In this study, the difference in defect formation rates for monolayer WS₂ and hBN-encapsulated structures was examined. To achieve this, the formation rate ratio of λ was investigated:

$$\lambda = \frac{\Gamma_{\text{freestanding}}}{\Gamma_{\text{hBN-encapsulated}}} = \exp\left(-\frac{E_{f, \text{freestanding}} - E_{f, \text{hBN-encapsulated}}}{k_B T}\right) \quad (8)$$

At a temperature of $T = 102$ K and with $E_{f, \text{freestanding}} - E_{f, \text{hBN-encapsulated}} = -0.09$ eV, the estimated value of λ is approximately 10^{-4} . The Monte Carlo simulation was carried out based on the standard rejection MC algorithm⁶⁴. In each trial step, the time step is recorded inversely proportional to the reaction rate Q_k . Simulations consisting of 20,000-time steps each to achieve ideal defect saturation on the lattice were conducted.

Data availability

The Source Data underlying the figures of this study are available at <https://doi.org/10.6084/m9.figshare.25310755>. All raw data generated during the current study are available from the corresponding authors upon request.

Code availability

The custom code used in this study is available on Zenodo at <https://doi.org/10.5281/zenodo.13946075>.

References

- Aharonovich, I., Englund, D. & Toth, M. Solid-state single-photon emitters. *Nat. Photon.* **10**, 631–641 (2016).
- Aharonovich, I. & Toth, M. Quantum emitters in two dimensions. *Science* **358**, 170–171 (2017).
- Liu, X. & Hersam, M. C. 2D materials for quantum information science. *Nat. Rev. Mater.* **4**, 669–684 (2019).
- Klein, J. et al. Site-selectively generated photon emitters in monolayer MoS₂ via local helium ion irradiation. *Nat. Commun.* **10**, 2755 (2019).
- Palacios-Berraquero, C. et al. Large-scale quantum-emitter arrays in atomically thin semiconductors. *Nat. Commun.* **8**, 15093 (2017).
- Branny, A., Kumar, S., Proux, R. & Gerardot, B. D. Deterministic strain-induced arrays of quantum emitters in a two-dimensional semiconductor. *Nat. Commun.* **8**, 15053 (2017).
- Parto, K., Azzam, S. I., Banerjee, K. & Moody, G. Defect and strain engineering of monolayer WSe₂ enables site-controlled single-photon emission up to 150 K. *Nat. Commun.* **12**, 3585 (2021).
- Klein, J. et al. Engineering the luminescence and generation of individual defect emitters in atomically thin MoS₂. *ACS Photon.* **8**, 669–677 (2021).
- Kianinia, M., Xu, Z.-Q., Toth, M. & Aharonovich, I. Quantum emitters in 2D materials: Emitter engineering, photophysics, and integration in photonic nanostructures. *Appl. Phys. Rev.* **9**, 011306 (2022).
- Shotan, Z. et al. Photoinduced modification of single-photon emitters in hexagonal boron nitride. *ACS Photon.* **3**, 2490–2496 (2016).
- Tran, T. T., Bradac, C., Solntsev, A. S., Toth, M. & Aharonovich, I. Suppression of spectral diffusion by anti-Stokes excitation of quantum emitters in hexagonal boron nitride. *Appl. Phys. Lett.* **115**, 071102 (2019).
- Efros, A. L. & Nesbitt, D. J. Origin and control of blinking in quantum dots. *Nat. Nanotechnol.* **11**, 661–671 (2016).
- Srivastava, A. et al. Optically active quantum dots in monolayer WSe₂. *Nat. Nanotechnol.* **10**, 491–496 (2015).
- Tonndorf, P. et al. Single-photon emission from localized excitons in an atomically thin semiconductor. *Optica* **2**, 347–352 (2015).
- Mitterreiter, E. et al. The role of chalcogen vacancies for atomic defect emission in MoS₂. *Nat. Commun.* **12**, 3822 (2021).
- Tongay, S. et al. Defects activated photoluminescence in two-dimensional semiconductors: interplay between bound, charged and free excitons. *Sci. Rep.* **3**, 2657 (2013).
- Feng, J. et al. Imaging of optically active defects with nanometer resolution. *Nano Lett.* **18**, 1739–1744 (2018).
- Bourrellier, R. et al. Bright UV single photon emission at point defects in h-BN. *Nano Lett.* **16**, 4317–4321 (2016).
- De Graaf, S., Ahmadi, M., Lazić, I., Bosch, E. G. & Kooi, B. J. Imaging atomic motion of light elements in 2D materials with 30 kV electron microscopy. *Nanoscale* **13**, 20683–20691 (2021).
- de Graaf, S. & Kooi, B. J. Radiation damage and defect dynamics in 2D WS₂: a low-voltage scanning transmission electron microscopy study. *2D Mater.* **9**, 015009 (2022).
- Calderon V, S. et al. Atomic electrostatic maps of point defects in MoS₂. *Nano Lett.* **21**, 10157–10164 (2021).
- Zhou, W. et al. Intrinsic structural defects in monolayer molybdenum disulfide. *Nano Lett.* **13**, 2615–2622 (2013).
- Schieber, J., Krinsley, D. & Riciputi, L. Diagenetic origin of quartz silt in mudstones and implications for silica cycling. *Nature* **406**, 981–985 (2000).
- Shubina, T. V. et al. Mie resonances, infrared emission, and the band gap of InN. *Phys. Rev. Lett.* **92**, 117407 (2004).
- Niioaka, H. et al. Multicolor cathodoluminescence microscopy for biological imaging with nanophosphors. *Appl. Phys. Express* **4**, 112402 (2011).
- Kociak, M. & Zagonel, L. F. Cathodoluminescence in the scanning transmission electron microscope. *Ultramicroscopy* **176**, 112–131 (2017).
- Singh, A., Lee, H. Y. & Građečak, S. Direct optical-structure correlation in atomically thin dichalcogenides and heterostructures. *Nano Res.* **13**, 1363–1368 (2020).
- Lee, H. Y. et al. Strong and localized luminescence from interface bubbles between stacked hBN multilayers. *Nat. Commun.* **13**, 5000 (2022).
- Hayee, F. et al. Revealing multiple classes of stable quantum emitters in hexagonal boron nitride with correlated optical and electron microscopy. *Nat. Mater.* **19**, 534–539 (2020).
- Zhang, Z. et al. Optically active chalcogen vacancies in monolayer semiconductors. *Adv. Opt. Mater.* **10**, 2201350 (2022).
- Turunen, M. et al. Quantum photonics with layered 2D materials. *Nat. Rev. Phys.* **4**, 219–236 (2022).
- Palacios-Berraquero, C. et al. Atomically thin quantum light-emitting diodes. *Nat. Commun.* **7**, 12978 (2016).
- Zheng, S. et al. Giant enhancement of cathodoluminescence of monolayer transitional metal dichalcogenides semiconductors. *Nano Lett.* **17**, 6475–6480 (2017).
- Tran, T. T., Bray, K., Ford, M. J., Toth, M. & Aharonovich, I. Quantum emission from hexagonal boron nitride monolayers. *Nat. Nanotechnol.* **11**, 37–41 (2016).
- Jungwirth, N. R. et al. Temperature dependence of wavelength selectable zero-phonon emission from single defects in hexagonal boron nitride. *Nano Lett.* **16**, 6052–6057 (2016).
- Singla, S. et al. Probing correlation of optical emission and defect sites in hexagonal boron nitride by high-resolution STEM-EELS. *Nano Lett.* **24**, 9212–9220 (2024).
- Cho, Y. & Berkelbach, T. C. Environmentally sensitive theory of electronic and optical transitions in atomically thin semiconductors. *Phys. Rev. B* **97**, 041409 (2018).
- Wang, Y. et al. Spin-valley locking effect in defect states of monolayer MoS₂. *Nano Lett.* **20**, 2129–2136 (2020).
- Schuler, B. et al. Large spin-orbit splitting of deep in-gap defect states of engineered sulfur vacancies in monolayer WS₂. *Phys. Rev. Lett.* **123**, 076801 (2019).
- Komsa, H.-P., Kurasch, S., Lehtinen, O., Kaiser, U. & Krasheninnikov, A. V. From point to extended defects in two-dimensional MoS₂: evolution of atomic structure under electron irradiation. *Phys. Rev. B* **88**, 035301 (2013).
- Xiao, C. et al. Mechanisms of electron-beam-induced damage in perovskite thin films revealed by cathodoluminescence spectroscopy. *J. Phys. Chem. C* **119**, 26904–26911 (2015).
- Senesi, G. S., Harmon, R. S. & Hark, R. R. Field-portable and handheld laser-induced breakdown spectroscopy: Historical review, current status and future prospects. *Spectrochim. Acta Part B At. Spectrosc.* **175**, 106013 (2021).
- Rosenberger, M. R., Chuang, H.-J., McCreary, K. M., Li, C. H. & Jonker, B. T. Electrical characterization of discrete defects and impact of defect density on photoluminescence in monolayer WS₂. *ACS Nano* **12**, 1793–1800 (2018).
- Bozheyev, F. et al. Pulsed cathodoluminescence of WS₂ nanocrystals at various electron excitation energy densities: defect induced sub-band gap emission. *J. Lumin.* **192**, 1308–1312 (2017).
- Zhao, Y. et al. Electrical spectroscopy of defect states and their hybridization in monolayer MoS₂. *Nat. Commun.* **14**, 44 (2023).
- Zhang, X. et al. Hidden vacancy benefit in monolayer 2D semiconductors. *Adv. Mater.* **33**, 2007051 (2021).

47. Pizzocchero, F. et al. The hot pick-up technique for batch assembly of van der Waals heterostructures. *Nat. Commun.* **7**, 11894 (2016).
 48. Huang, X. et al. Tracking cubic ice at molecular resolution. *Nature* **617**, 86–91 (2023).
 49. Zhu, L. et al. Visualizing anisotropic oxygen diffusion in ceria under activated conditions. *Phys. Rev. Lett.* **124**, 056002 (2020).
 50. Egerton, R. F., Li, P. & Malac, M. Radiation damage in the TEM and SEM. *Micron* **35**, 399–409 (2004).
 51. Xin, H. L. & Muller, D. A. Aberration-corrected ADF-STEM depth sectioning and prospects for reliable 3D imaging in S/TEM. *Microscopy* **58**, 157–165 (2009).
 52. Tian, X. et al. Correlating the three-dimensional atomic defects and electronic properties of two-dimensional transition metal dichalcogenides. *Nat. Mater.* **19**, 867–873 (2020).
 53. Koch, C. T. *Determination of Core Structure Periodicity and Point Defect Density along Dislocations* (Arizona State University, 2002).
 54. Chen, T. & Guestrin, C. XGBoost: A Scalable Tree Boosting System. *Proceedings of the 22nd ACM SIGKDD International Conference on Knowledge Discovery and Data Mining*. San Francisco, California, USA. 785–794 (Association for Computing Machinery, 2016).
 55. Pedregosa, F. et al. Scikit-learn: machine learning in Python. *J. Mach. Learn. Res.* **12**, 2825–2830 (2011).
 56. Momma, K. & Izumi, F. VESTA 3 for three-dimensional visualization of crystal, volumetric and morphology data. *J. Appl. Crystallogr.* **44**, 1272–1276 (2011).
 57. Alkauskas, A., Buckley, B. B., Awschalom, D. D. & Van de Walle, C. G. First-principles theory of the luminescence lineshape for the triplet transition in diamond NV centres. *N. J. Phys.* **16**, 073026 (2014).
 58. Henkelman, G., Uberuaga, B. P. & Jónsson, H. A climbing image nudged elastic band method for finding saddle points and minimum energy paths. *J. Chem. Phys.* **113**, 9901–9904 (2000).
 59. Henkelman, G. & Jónsson, H. Improved tangent estimate in the nudged elastic band method for finding minimum energy paths and saddle points. *J. Chem. Phys.* **113**, 9978–9985 (2000).
 60. Grimme, S., Antony, J., Ehrlich, S. & Krieg, H. A consistent and accurate ab initio parametrization of density functional dispersion correction (DFT-D) for the 94 elements H–Pu. *J. Chem. Phys.* **132**, 154104 (2010).
 61. Wang, Y. & Windl, W. Native point defects from stoichiometry-linked chemical potentials in cubic boron arsenide. *J. Appl. Phys.* **129**, 075703 (2021).
 62. Jain, A. et al. Commentary: The Materials Project: a materials genome approach to accelerating materials innovation. *APL Mater.* **1**, 011002 (2013).
 63. Kiecicka, D. et al. Defects in WS₂ monolayer calculated with a non-local functional: any difference from GGA? *Electron. Struct.* **5**, 024001 (2023).
 64. Serebrinsky, S. A. Physical time scale in kinetic Monte Carlo simulations of continuous-time Markov chains. *Phys. Rev. E—Stat. Nonlinear Soft Matter Phys.* **83**, 037701 (2011).
- (XDB33030200 (X.B.), and YSBRO47 (S.M.)). L.W. is grateful for the support from the Youth Innovation Promotion Association of CAS (2020009).

Author contributions

L.W. and X.B. conceived the idea and supervised the project. H.S. conducted the STEM-CL experiments, HAADF and STEM-iDPC experiments supervised by L.W. and X.B. H.S. and L.W. analyzed the data. L. Liao and C.C. programmed for data processing and plotting. hBN|WS₂|hBN heterostructure was prepared with the assistance of M.D.; Q.Y. and J.W. carried out the DFT calculation advised by S.M.; M.C. programmed machine learning algorithms for data analysis and carried out the DFT calculation advised by J.C. and L. Liu; Z.C., L. Liao, X.H., and Z.W. helped data analysis. Z.X., W.W., K.L., L.W., and X.B. built the experimental setup. H.S. and L.W. wrote the manuscript with contributions from all coauthors. All the authors discussed the results and commented on the manuscript.

Competing interests

The authors declare no competing interests.

Additional information

Supplementary information The online version contains supplementary material available at <https://doi.org/10.1038/s41467-024-53880-4>.

Correspondence and requests for materials should be addressed to Xuedong Bai, Ji Chen, Sheng Meng or Lifan Wang.

Peer review information *Nature Communications* thanks Soumya Sarkar, and the other, anonymous, reviewers for their contribution to the peer review of this work. A peer review file is available.

Reprints and permissions information is available at <http://www.nature.com/reprints>

Publisher's note Springer Nature remains neutral with regard to jurisdictional claims in published maps and institutional affiliations.

Open Access This article is licensed under a Creative Commons Attribution-NonCommercial-NoDerivatives 4.0 International License, which permits any non-commercial use, sharing, distribution and reproduction in any medium or format, as long as you give appropriate credit to the original author(s) and the source, provide a link to the Creative Commons licence, and indicate if you modified the licensed material. You do not have permission under this licence to share adapted material derived from this article or parts of it. The images or other third party material in this article are included in the article's Creative Commons licence, unless indicated otherwise in a credit line to the material. If material is not included in the article's Creative Commons licence and your intended use is not permitted by statutory regulation or exceeds the permitted use, you will need to obtain permission directly from the copyright holder. To view a copy of this licence, visit <http://creativecommons.org/licenses/by-nc-nd/4.0/>.

© The Author(s) 2024

Acknowledgements

This work was supported by the National Natural Science Foundation of China (51991344 (X.B.), 12334001 (X.B.), 52322311 (L.W.), 12025407 (S.M.), and 52025023 (K.L.)), National Key R&D Program of China (2021YFA1400500 (L.L.), 2019YFA0307800 (L.L.), 2021YFA1400204 (S.M.) and 2021YFA1400502 (K.L.)), and Chinese Academy of Sciences